Available online at www.sciencedirect.com
ScienceDirect
Comput. Methods Appl. Mech. Engrg. 360 (2020) 112704
Computer methods in applied mechanics and engineering
www.elsevier.com/locate/cma

On the BFGS monolithic algorithm for the unified phase field damage theory

Jian-Ying Wu[a,*], Yuli Huang[b], Vinh Phu Nguyen[c]

[a] *State Key Laboratory of Subtropical Building Science, South China University of Technology, 510641 Guangzhou, China*
[b] *Arup, 560 Mission Street, Suite 700, San Francisco, CA 94105, United States*
[c] *Department of Civil Engineering, Monash University, Clayton, Victoria 3800, Australia*

Received 5 July 2019; received in revised form 21 August 2019; accepted 18 October 2019
Available online 31 October 2019

Abstract

Despite the popularity in modeling complex and arbitrary crack configurations in solids, phase-field damage models suffer from burdensome computational cost. This issue arises largely due to the robust but inefficient alternating minimization (AM) or staggered algorithm usually employed to solve the coupled damage–displacement governing equations. Aiming to tackle this difficulty, we propose in this work, *for the first time*, to use the Broyden–Fletcher–Goldfarb–Shanno (BFGS) algorithm to solve in a monolithic manner the system of coupled governing equations, rather than the standard Newton one which is notoriously poor for problems involving non-convex energy functional. It is found that, the BFGS algorithm yields identical results to the AM/staggered solver, and is also robust for both brittle fracture and quasi-brittle failure with a single or multiple cracks. However, much less iterations are needed to achieve convergence. Furthermore, as the system matrix is less reformed per increment, the quasi-Newton monolithic algorithm is much more efficient than the AM/staggered solver. Representative numerical examples show that the saving in CPU time is about factor 3∼7, and the larger the problem is, the more saving it gains. As the BFGS monolithic algorithm has been incorporated in many commercial software packages, it can be easily implemented and is thus attractive in the phase-field damage modeling of localized failure in solids.

Keywords: Phase-field; Damage; Fracture; BFGS method; Monolithic algorithm; Staggered solver

1. Introduction

During the last two decades, phase-field damage models have been very popular in the computational modeling of complex fracture problems; see [1] and [2] for the reviews. This popularity is attributed largely to their intrinsic capability in dealing with complex crack configurations involving arbitrary nucleation, propagation, branching or merging in a single standard-alone framework, with no need of any *ad hoc* criterion or extrinsic tracking algorithm. The magic comes, on the one hand, from the variational approach to fracture set forth by Francfort and Marigo [3], and on the other hand, from the numerically more amenable counterpart [4,5] based on the Ambrosio and Tortorelli [6] elliptic regularization. That is, a cracking solid Ω is completely described by a pair of state variables containing

* Corresponding author.
E-mail address: jywu@scut.edu.cn (J.-Y. Wu).

https://doi.org/10.1016/j.cma.2019.112704

the displacement field $\boldsymbol{u}(\boldsymbol{x})$ and the crack (or damage) phase-field $d(\boldsymbol{x})$ which are determined by the following bound constrained optimization problem[1]

$$\big(\boldsymbol{u}(\boldsymbol{x}), d(\boldsymbol{x})\big) = \mathrm{Arg}\Big\{\min \mathscr{E}(\boldsymbol{u}, d)\Big\} \qquad \text{subjected to} \qquad \dot{d}(\boldsymbol{x}) \geq 0,\ d(\boldsymbol{x}) \in [0, 1] \tag{1.1}$$

for the time derivative $\dot{(\,)}$. The energy functional $\mathscr{E}$ of the cracking solid is characterized by two characteristic functions [10,11], i.e., an energetic degradation function $\omega(d)$ associated with the strain energy stored in the solid Ω and a geometric crack function $\alpha(d)$ for the regularized crack band $\mathcal{B}$

$$\mathscr{E}(\boldsymbol{u}, d) = \int_{\Omega} \psi(\boldsymbol{\epsilon}(\boldsymbol{u}), \omega(d))\, \mathrm{d}V + \int_{\mathcal{B}} G_{\mathrm{f}} \frac{1}{c_\alpha b}\Big[\alpha(d) + \big(b\big|\nabla d\big|\big)^2\Big]\, \mathrm{d}V \tag{1.2}$$

where $\boldsymbol{\epsilon} := \nabla^{\mathrm{sym}}\boldsymbol{u}$ is the infinitesimal strain field; G_{f} is the fracture toughness (energy), usually regarded as a material property; b is a length scale parameter regularizing the regularized crack band; $c_\alpha := 4\int_0^1 \sqrt{\alpha(\beta)}\, \mathrm{d}\beta$ is a scaling constant related to the geometric crack function $\alpha(d)$.

Various phase-field damage models differ in the characteristic functions. In the standard version proposed by Bourdin et al. [4,5] and modified by Miehe et al. [12], the quadratic functions $\omega(d) = \big(1-d\big)^2$ and $\alpha(d) = d^2$ are used. Though the resulting `AT2` model has been widely applied, it lacks an elastic stage. In other words, once the load is applied, no matter how low the value is, damage nucleates and the global response is nonlinear from the very beginning. In order to achieve an elastic response prior to the peak load, Pham et al. [13] proposed the `AT1` model with a linear geometric function $\alpha(d) = d$. Note that other alternatives exist in, e.g., [14] and [15] in which energetic functions of cubic and quartic polynomials are adopted, respectively, with the quadratic geometric function $\alpha(d) = d^2$ preserved.

Most phase-field damage models apply only to brittle fracture with very few exceptions. The `AT2` model was first extended to cohesive fracture in [5] and later elaborated in [16], [17], [18] and Nguyen et al. [19]. However, only interfacial cracks propagating along pre-defined paths can be dealt with. Another noteworthy exception is the phase-field damage model developed by Conti et al. [20] and Focardi and Iurlano [21] for cohesive fracture. However, the global response is heavily dependent on the length scale parameter b and general softening laws cannot be considered.

More recently, Wu [10,11] and Wu and Nguyen [22] proposed a unified phase-field damage theory which applies to both brittle fracture and quasi-brittle failure. It is characterized by a generic rational energetic function $\omega(d)$ and a parametrized polynomial geometric one $\alpha(d)$. The aforementioned `AT1` and `AT2` models are both incorporated as the particular examples. More importantly, a pair of optimal functions for cohesive fracture are determined upon the strain localization analysis of the resulting phase-field model. With all the involved parameters calibrated from the standard material properties (i.e., Young's modulus, failure strength and fracture energy), those softening laws frequently adopted in the discontinuous cohesive zone model (CZM) [23], e.g., the linear one, the exponential one, and the Cornelissen et al. [24] one, etc., can be reproduced or approximated with high precision. Therefore, it is named as the phase-field regularized cohesive zone model, or in short, PF-CZM. Remarkably, the global response given by the PF-CZM is not only independent of the mesh size/alignment [25], but also insensitive to the length scale parameter b for both static fracture [11,26,27] and dynamic fracture [28], which is not the case for other phase-field damage models.

A big complaint of phase-field damage models is the burdensome computational cost. On the one hand, the inefficiency is caused by the high resolution necessary to resolve the damage gradient ∇d associated with the highly non-uniformly distributed damage profile $d(\boldsymbol{x})$. This weakness can be tackled by mesh adaptation strategies [15,29], in particular, the anisotropic one suggested in [30], [31] and [32]. On the other hand, the standard Newton method based monolithic solver performs rather poor and usually fails for the non-convex energy functional (1.2) with respect to the unknowns $(\boldsymbol{u}, d)$. Though a few attempts [29,33–37] have been proposed to deal with this issue, the alternating minimization (AM) or staggered solver [4,5] seems to be the only one that is robust enough to solve the coupled damage–displacement governing equation. However, the AM/staggered solver is extremely slow and it is

[1] Here we limit ourselves only to the relevant studies from the computational mechanics community and therefore, those phase-field models developed by the physics community, e.g., [7] and [8], etc., are not considered. The interested reader can refer to Spatschek et al. [9] for the review from the physics community.

not unusual that more than 1000 iterations are needed to achieve convergence for some critical incremental steps. Another option is to use the explicit algorithm as in [38], but the numerical stability issue cannot be easily tackled.

Aiming to remedy the computational overheads brought about by the second weakness, in this work we propose using a quasi-Newton method based monolithic algorithm for the unified phase-field damage theory. More specifically, the Broyden–Fletcher–Goldfarb–Shanno (BFGS) algorithm is employed to solve the coupled governing equations resulting from phase-field damage models. Representative numerical examples show that, the BFGS algorithm is not only robust for both brittle fracture and quasi-brittle failure, but also much more efficient compared to the AM/staggered solver. Therefore, it is rather attractive in the phase-field damage modeling of localized failure in solids.

The remaining of the paper is organized as follows. Section 2 recalls briefly the theoretic aspect and the finite element implementation of the unified phase-field damage theory, with the `AT1`, `AT2` and `PF-CZM` all being incorporated as particular examples. Section 3 presents three numerical algorithms in solving the coupled governing equations. After the Newton monolithic algorithm and the AM/staggered solver are discussed, the BFGS quasi-Newton method is addressed. Section 4 compares numerically the proposed BFGS monolithic algorithm against the AM/staggered solver by several representative benchmark examples. The relevant conclusions are drawn in Section 5.

Notation. Compact tensor notation is used in the theoretical part of this paper. As general rules, scalars are denoted by italic light-face Greek or Latin letters (e.g. a or λ); vectors, second- and fourth-order tensors are signified by italic boldface minuscule, majuscule and blackboard-bold majuscule characters like $\boldsymbol{a}$, $\boldsymbol{A}$ and $\mathbb{A}$, respectively. The inner products with single and double contractions are denoted by '$\cdot$' and ':', respectively. In the finite element implementation, Voigt notation is adopted where vectors and second-order tensors are denoted by boldface minuscule and majuscule letters like $\mathbf{a}$ and $\mathbf{A}$, respectively.

2. A brief summary of the unified phase-field damage theory

As shown in Fig. 1(a), the reference configuration of a cracking solid $\Omega \subset \mathbb{R}^{n_{\text{dim}}}$ ($n_{\text{dim}} = 1, 2, 3$) with a sharp crack set $\mathcal{S} \subset \mathbb{R}^{n_{\text{dim}}-1}$ is considered. The external boundary is signified by $\partial\Omega \subset \mathbb{R}^{n_{\text{dim}}-1}$ and the outward unit normal vector is denoted by $\boldsymbol{n}$. The solid is kinematically characterized by the displacement field $\boldsymbol{u}(\boldsymbol{x})$, with the material particles labeled by their spatial coordinates $\boldsymbol{x}$. Upon the assumption of infinitesimal deformations, the strain field is given by $\boldsymbol{\epsilon} := \nabla^{\text{sym}}\boldsymbol{u}$, for the symmetric gradient operator $\nabla^{\text{sym}}(\cdot)$ with respect to the spatial coordinates $\boldsymbol{x}$. Assume that the solid is subjected to specific body forces (per unit mass) $\boldsymbol{b}^*$, while prescribed surface tractions $\boldsymbol{t}^*$ and displacements $\boldsymbol{u}^*$ are applied to some part of the external boundary $\partial\Omega_t \subseteq \partial\Omega$ and the disjoint one $\partial\Omega_u \subseteq \partial\Omega$, respectively.

Within the framework of phase-field damage models [4,5,10–12], the sharp crack $\mathcal{S}$ is regularized over a localization band $\mathcal{B} \subseteq \Omega$ in which the crack phase-field or damage field $d(\boldsymbol{x})$ localizes, with the ourward unit normal vector denoted by $\boldsymbol{n}_{\mathcal{B}}$; see Fig. 1(b). Note that the measure of the localization band is characterized by a length scale parameter b that can be taken as small as possible. As in the classical continuum damage mechanics, $d(\boldsymbol{x}) = 0$ means the material is intact with no damage whereas $d(\boldsymbol{x}) = 1$ represents complete fracture. Similarly to the displacement field, Dirichlet boundary conditions, e.g., $d(\boldsymbol{x}) = 0$ in elastic domains and $d(\boldsymbol{x}) = 1$ on pre-defined cracks can be applied to the damage field as well. Note that the crack phase-field should satisfy the boundedness $d(\boldsymbol{x}) \in [0, 1]$ and the irreversibility (i.e., the unrecoverable property with self-healing excluded) $\dot{d}(\boldsymbol{x}) \geq 0$. Moreover, the localization band $\mathcal{B}$, usually a much smaller sub-domain of the computational domain Ω, is not known *a priori* but rather, it is determined and automatically updated.

2.1. Fundamental formulations

In accordance with Wu [10,11] and Wu and Nguyen [22], the fundamental formulations of the unified phase-field damage theory are summarized in Box I.

Though other expressions can be adopted as in [12] and Wu et al. [39], in this work the effective damage energy release rate (i.e., driving force) $\bar{Y} := \frac{1}{2}\bar{\sigma}_{\text{eq}}^2/E_0$ is defined in terms of an equivalent effective stress $\bar{\sigma}_{\text{eq}}$, with E_0

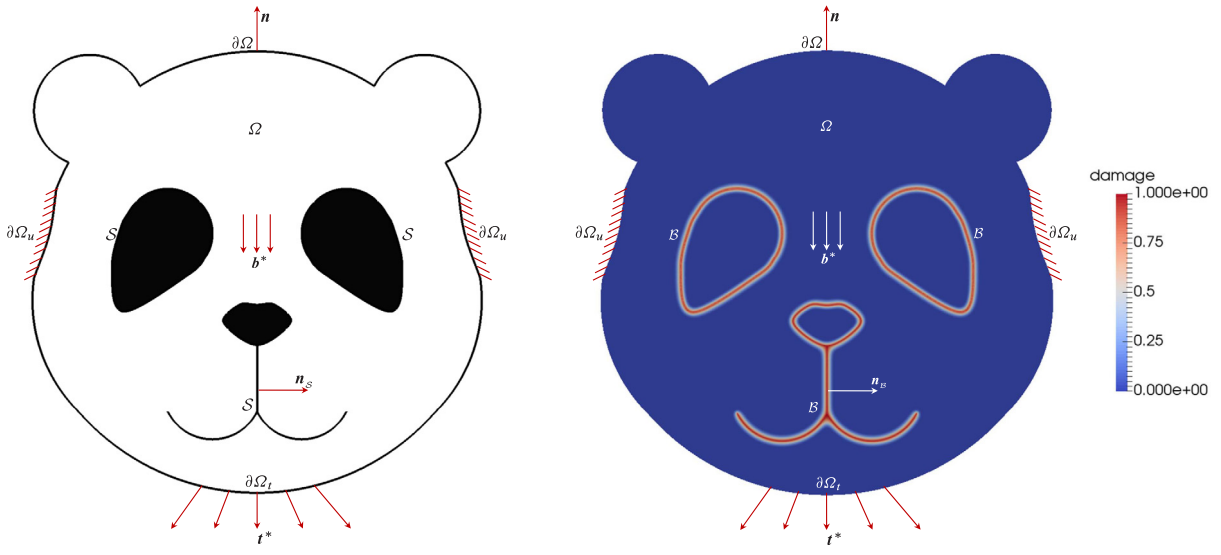

(a) A solid with sharp cracks and interfaces

(b) A solid with geometrically regularized cracks and interfaces

Fig. 1. A cracking solid with sharp cracks/interfaces and the geometric regularization.

Components	Governing equations	Constitutive relations	Characteristic functions
Displacement sub-problem	$\nabla \cdot \boldsymbol{\sigma} + \boldsymbol{b}^* = \boldsymbol{0}$ $\boldsymbol{\sigma} \cdot \boldsymbol{n} = \boldsymbol{t}^*$	$\boldsymbol{\sigma} = \omega(d)\bar{\boldsymbol{\sigma}}$ $Y = -\omega'(d)\bar{Y}$	$\omega(d) = \dfrac{(1-d)^p}{(1-d)^p + a_1 d \cdot P(d)}$ $P(d) = 1 + a_2 d + a_3 d^2 + \cdots$
Damage sub-problem[a]	$\nabla \cdot \boldsymbol{q} + Q(d) \le 0$ $\boldsymbol{q} \cdot \boldsymbol{n}_{\mathcal{B}} \ge 0$	$\boldsymbol{q} = \dfrac{2b}{c_\alpha} G_{\mathrm{f}} \nabla d$ $Q = Y - \dfrac{G_{\mathrm{f}}}{c_\alpha b} \alpha'(d)$	$\alpha(d) = \xi d + (1-\xi) d^2$ $c_\alpha = 4 \int_0^1 \sqrt{\alpha(\beta)}\, \mathrm{d}\beta$

[a]The conditions $\dot{d} \ge 0$ and $d \in [0, 1]$ have to be fulfilled.

Box I. The unified phase-field damage theory for fracture.

being Young's modulus. For tension dominant failure brittle and quasi-brittle materials, the following definitions can be considered for $\bar{\sigma}_{\mathrm{eq}}$

$$\bar{\sigma}_{\mathrm{eq}}(\bar{\boldsymbol{\sigma}}) = \begin{cases} \langle \bar{\sigma}_1 \rangle & \text{Rankine criterion} \\ \dfrac{\rho_c - 1}{2\rho_c} \bar{I}_1 + \dfrac{1}{2\rho_c} \sqrt{(\rho_c - 1)^2 \bar{I}_1^2 + 12\rho_c \bar{J}_2} & \text{modified von Mises criterion} \end{cases} \tag{2.1}$$

where $\bar{\sigma}_1$ and $\bar{I}_1$ represent the major principal value and the first invariant of the effective stress tensor $\bar{\boldsymbol{\sigma}} := \mathbb{E}_0 : \boldsymbol{\epsilon}$, respectively, with $\mathbb{E}_0$ being the fourth-order elasticity tensor; $\bar{J}_2 := \frac{1}{2}\bar{\boldsymbol{\sigma}} : \bar{\boldsymbol{\sigma}} - \frac{1}{6}\bar{I}_1^2$ denotes the second invariant of the effective deviatoric stress tensor; $\rho_c := f_c / f_t$ is the strength ratio between the uniaxial compressive strength f_c

Models	ξ	c_α	p	a_1	a_2	a_3
AT2	0	2	2	2	$-\frac{1}{2}$	0
AT1	1	$\frac{8}{3}$	2	2	$-\frac{1}{2}$	0
PF-CZM	2	π	≥ 2	$\frac{4}{\pi}\frac{l_{\text{ch}}}{b}$	$2\beta_k^{\frac{2}{3}} - \left(p+\frac{1}{2}\right)$	$\begin{cases} 0 & p>2 \\ \frac{1}{2}\beta_w^2 - (1+a_2) & p=2 \end{cases}$

Box II. Various phase-field damage models for fracture.

and the uniaxial tensile one f_t. This modified von Mises criterion was first used in [40] in the context of phase-field damage models.

Regarding the parameters involved in the generic energetic degradation function $\omega(d)$ and the parametrized geometric crack function $\alpha(d)$, several phase-field damage models are recovered as in Box II. In this box, AT2 and AT1 refer to the phase-field damage models proposed in [4] and in [13], respectively, following the notations introduced in [41]. As the energetic degradation function $\omega(d) = \left(1-d\right)^2$ depends solely on the crack phase-field, both models apply only to brittle fracture. Moreover, though the AT1 exhibits a linear elastic stage prior to the peak strength, the numerical results given by both models are sensitive to the incorporated length scale parameter b; see [25].

PF-CZM refers to the phase-field regularized cohesive zone model (CZM) proposed by Wu [10,11] and Wu and Nguyen [22] which can deal with both brittle and quasi-brittle fracture. Moreover, the numerical result is insensitive to the incorporated length scale parameter, provided the latter is small enough to resolve the non-uniformly distributed damage field. With a set of properly calibrated parameters $p \geq 2$, a_2 and a_3, general softening laws of the discontinuous CZM [23] can be reproduced or approximated with high precision. Here, Irwin's characteristic length is defined as $l_{\text{ch}} := E_0 G_{\text{f}}/f_t^2$, with f_t and G_{f} being the failure strength and fracture energy (toughness), respectively. Ratios β_k and β_w compare the initial slope k_0 and the limit crack opening w_c of the target traction–separation law (TSL) to those of the linear softening curve, i.e.,

$$\beta_k := \frac{k_0}{-\frac{1}{2}f_t^2/G_{\text{f}}} \geq 1, \qquad \beta_w := \frac{w_c}{2G_{\text{f}}/f_t}$$

For those softening curves frequently adopted for brittle and quasi-brittle solids, it follows that [10,11,22]

$$\begin{cases} \text{Linear softening curve:} & p=2.0,\ a_2=-\frac{1}{2}, & a_3=0 \\ \text{Exponential softening curve:} & p=2.5,\ a_2=2^{5/3}-3, & a_3=0 \\ \text{Cornelissen et al. [24] softening curve:} & p=2.0,\ a_2=1.3868, & a_3=0.9106 \end{cases} \tag{2.2}$$

Other softening curves can be considered as well [42].

2.2. Dealing with damage irreversibility

In phase-field models, the damage field variable $d(\boldsymbol{x})$ has to satisfy the irreversibility condition $\dot{d} \geq 0$. One option is to enforce this condition by using a bound constrained optimization solver like the so-called "reduced-space active set Newton method" [43] as in [44], [37] and [26]. Other options include the (augmented) Lagrangian and penalty methods, but the former introduces extra variables [45] while the latter is prone to stability issues unless the penalty constants are carefully selected as in [46].

In this work, the implicit method suggested by Miehe et al. [12] is followed. That is, a history variable $\mathcal{H}$ is introduced to represent the maximum value of the effective damage driving force $\bar{Y}$ ever reached, i.e.,

$$\mathcal{H} = \max_{n\in[0,T]}\left(\bar{Y}_0, \bar{Y}_n\right), \qquad \bar{Y}_0 = \frac{1}{2E_0}f_t^2 \tag{2.3}$$

for the value $\bar{Y} = \frac{1}{2}\bar{\sigma}_{\text{eq}}^2/E_0$ at current instant $T_n \in [0, T]$.

Accordingly, the damage evolution law becomes an equality [27]

$$\nabla \cdot \boldsymbol{q} + Q(d) = 0 \tag{2.4}$$

where the damage source term $Q(d)$ is replaced by

$$Q(d) = -\omega'(d)\mathcal{H} - \frac{G_{\text{f}}}{c_\alpha b}\alpha'(d) \tag{2.5}$$

In this way, the irreversibility condition $\dot{d}(\boldsymbol{x}) \geq 0$ and non-negative damage field $d(\boldsymbol{x}) \geq 0$ can be sufficiently guaranteed.

Note that the condition $d \leq 1.0$ is seldom violated [25] and is therefore not specially dealt with in this work.

2.3. Weak form of the governing equations

Let us introduce the following trial spaces of the displacement and damage fields

$$\mathscr{U} := \left\{\boldsymbol{u} \middle| \boldsymbol{u}(\boldsymbol{x}) \in \left[H^1(\Omega)\right]^{n_{\text{dim}}},\ \boldsymbol{u}(\boldsymbol{x}) = \boldsymbol{u}^*\ \forall \boldsymbol{x} \in \partial\Omega_u\right\} \tag{2.6a}$$

$$\bar{\mathscr{U}} := \left\{d \middle| d(\boldsymbol{x}) \in H^1(\Omega)\ \forall \boldsymbol{x} \in \mathcal{B}\right\} \tag{2.6b}$$

where $[H^1(\Omega)]^{n_{\text{dim}}}$ denotes the Sobolev space of vector fields defined in the solid $\Omega \subset \mathbb{R}^{n_{\text{dim}}}$. In accordance with the weighted residual method, the weak form of the governing equations is expressed as: Find $\boldsymbol{u} \in \mathscr{U}$ and $d \in \bar{\mathscr{U}}$ such that

$$\begin{cases} \displaystyle\int_\Omega \boldsymbol{\sigma} : \nabla^{\text{sym}}\delta\boldsymbol{u}\ \mathrm{d}V = \delta\mathscr{P} & \forall\delta\boldsymbol{u} \in \mathscr{V} \\ \displaystyle\int_{\mathcal{B}} \boldsymbol{q} \cdot \nabla\delta d\ \mathrm{d}V - \int_{\mathcal{B}} Q\delta d\ \mathrm{d}V = 0 & \forall\delta d \in \bar{\mathscr{V}} \end{cases} \tag{2.7}$$

where we have introduced the following test spaces

$$\mathscr{V} := \left\{\delta\boldsymbol{u} \middle| \boldsymbol{u}(\boldsymbol{x}) \in \left[H^1(\Omega)\right]^{n_{\text{dim}}},\ \delta\boldsymbol{u}(\boldsymbol{x}) = \boldsymbol{0}\ \forall \boldsymbol{x} \in \partial\Omega_u\right\} \tag{2.8a}$$

$$\bar{\mathscr{V}} := \left\{\delta d \middle| \delta d(\boldsymbol{x}) \in H^1(\Omega),\ \forall \boldsymbol{x} \in \mathcal{B}\right\} \tag{2.8b}$$

and the virtual power $\delta\mathscr{P}$

$$\delta\mathscr{P} = \int_\Omega \boldsymbol{b}^* \cdot \delta\boldsymbol{u}\ \mathrm{d}V + \int_{\partial\Omega_t} \boldsymbol{t}^* \cdot \delta\boldsymbol{u}\ \mathrm{d}A \tag{2.9}$$

associated with the external forces.

2.4. Finite element equilibrium equations

The weak forms (2.7) are usually discretized using multi-field finite elements. For the sake of simplicity, only 2D cases are considered but the extension to general 3D cases is straightforward. In this case, either the triangular piecewise linear element [10,11,13] or the quadrilateral bilinear one [47,48] can be considered, and each element node has three nodal degrees of freedom (dofs): two for the displacement and one for the damage.

The displacement field $\mathbf{u}^h$ and damage field d^h are interpolated as

$$\mathbf{u}^h(\boldsymbol{x}) = \sum_{I \in \mathscr{A}} \mathbf{N}_I(\boldsymbol{x})\ \mathbf{a}_I = \mathbf{N}\mathbf{a}, \qquad d^h(\boldsymbol{x}) = \sum_{J \in \mathscr{A}^*} \bar{N}_J(\boldsymbol{x})\ \bar{a}_J = \bar{\mathbf{N}}\bar{\mathbf{a}} \tag{2.10}$$

where the interpolation matrix $\mathbf{N} := \left[N_I\mathbf{I}\right]$ is associated with the nodal displacement dofs $\mathbf{a} := \left\{\mathbf{a}_I\right\}^{\text{T}}$ of all elements nodes $I \in \mathscr{A}$ in the computational domain Ω^h; the matrix $\bar{\mathbf{N}} := \left[\bar{N}_J\right]$ corresponds to the nodal damage dofs $\bar{\mathbf{a}} := \left\{\bar{a}_J\right\}^{\text{T}}$ of element nodes $J \in \mathscr{A}^*$ within the localization band $\mathcal{B}^h$. Though distinct interpolation functions can be considered, usually identical ones, i.e., $\bar{N}_J(\boldsymbol{x}) = N_J(\boldsymbol{x})$, are adopted in approximation of the displacement and

damage fields. Note that though the localization band $\mathcal{B}^h \subset \Omega^h$ can be coincident with the whole computational domain Ω^h, a much smaller sub-domain is in general considered, so long as it encompasses potential crack propagation paths; see [27] for more discussion.

The resulting strain field $\boldsymbol{\epsilon}^h$ and damage gradient ∇d^h are then given by

$$\boldsymbol{\epsilon}^h(\boldsymbol{x}) = \sum_{I \in \mathscr{A}} \mathbf{B}_I(\boldsymbol{x})\, \mathbf{a}_I = \mathbf{B}\mathbf{a}, \qquad \nabla d^h(\boldsymbol{x}) = \sum_{J \in \mathscr{A}^*} \bar{\mathbf{B}}_J(\boldsymbol{x})\, \bar{a}_J = \bar{\mathbf{B}}\bar{\mathbf{a}} \tag{2.11}$$

for the standard displacement–strain matrix $\mathbf{B} = \left[\boldsymbol{B}_I\right]$ and damage-gradient operator $\bar{\mathbf{B}} = \left[\bar{\mathbf{B}}_J\right]$, respectively. In 2-D cases, it follows that

$$\mathbf{B}_I(\boldsymbol{x}) = \begin{bmatrix} \partial_x N_I & 0 \\ 0 & \partial_y N_I \\ \partial_y N_I & \partial_x N_I \end{bmatrix} \qquad \bar{\mathbf{B}}_J(\boldsymbol{x}) = \begin{Bmatrix} \partial_x \bar{N}_J \\ \partial_y \bar{N}_J \end{Bmatrix} \tag{2.12}$$

Similarly expressions can be given for general 3-D cases.

With the above finite element discretization, the weak forms (2.7) yield the following generic residual equation

$$\mathbf{g}(\mathbf{z}) = \mathbf{0} \tag{2.13}$$

or, more specifically,

$$\mathbf{r} := \mathbf{f}^{\text{ext}} - \int_{\Omega} \mathbf{B}^{\mathrm{T}} \boldsymbol{\sigma}\, \mathrm{d}V = \mathbf{0} \tag{2.14a}$$

$$\bar{\mathbf{r}} := \int_{\mathcal{B}} \bar{\mathbf{N}}^{\mathrm{T}} Q \mathrm{d}V - \int_{\mathcal{B}} \bar{\mathbf{B}}^{\mathrm{T}} \boldsymbol{q}\, \mathrm{d}V = \mathbf{0} \tag{2.14b}$$

for the nodal unknowns $\mathbf{z} := \left\{\mathbf{a}, \bar{\mathbf{a}}\right\}$ and the standard external force vector $\mathbf{f}^{\text{ext}}$ [49].

Remark 2.1. Pre-defined cracks $\mathcal{S}$, if exist, can be accounted for either directly by mesh discretization or indirectly by the Dirichlet condition $d(\boldsymbol{x}) = 1$ for $\boldsymbol{x} \in \mathcal{S}$. The former strategy is adopted in this work. □

3. Numerical algorithms in solving the coupled governing equations

The system of nonlinear equations (2.14) is in general solved in an incremental procedure. That is, during the time interval $[0, T]$ of interest all the state variables are considered at the discrete interval $[t_n, t_{n+1}]$ for $n = 0, 1, 2, \ldots, N-1$. For a typical time increment $[t_n, t_{n+1}]$ of length $\Delta t := t_{n+1} - t_n$, the system of nonlinear equations (2.14) is solved with all state variables known at the instant t_n. The nodal unknowns are solved, usually in an iterative manner, for each incremental step until the end instant T is reached.

In this section, we present three numerical algorithms in solving the coupled governing equations (2.14). After the Newton monolithic algorithm and the alternating minimization solver, which are commonly adopted for coupled problems, are discussed, the Broyden–Fletcher–Goldfarb–Shanno (BFGS) method is addressed for the first time in the context of phase-field damage models.

3.1. Newton's monolithic algorithm

Let us first consider the Newton method based monolithic algorithm. In this algorithm, the residual equations (2.14) are linearized with respect to both unknowns $(\mathbf{a}, \bar{\mathbf{a}})$ using the Newton–Raphson method, leading to

$$\mathbf{g} + \frac{\partial \mathbf{g}}{\partial \mathbf{z}} \delta\mathbf{z} = \mathbf{g} - \mathbf{K}\delta\mathbf{z} = \mathbf{0}, \qquad \mathbf{K} := -\frac{\partial \mathbf{g}}{\partial \mathbf{z}} \tag{3.1}$$

or

$$\begin{bmatrix} \mathbf{K}_{uu} & \mathbf{K}_{ud} \\ \mathbf{K}_{du} & \mathbf{K}_{dd} \end{bmatrix} \begin{Bmatrix} \delta\mathbf{a} \\ \delta\bar{\mathbf{a}} \end{Bmatrix} = \begin{bmatrix} \mathbf{r} \\ \bar{\mathbf{r}} \end{bmatrix} \tag{3.2}$$

where the components of the stiffness matrix $\mathbf{K}$ are given by

$$\mathbf{K}_{uu} = \int_{\Omega} \mathbf{B}^{\mathrm{T}} \left(\frac{\partial \boldsymbol{\sigma}}{\partial \boldsymbol{\epsilon}}\right) \mathbf{B} \mathrm{d}V, \qquad \mathbf{K}_{ud} = \int_{\mathcal{B}} \mathbf{B}^{\mathrm{T}} \left(\frac{\partial \boldsymbol{\sigma}}{\partial d}\right) \bar{\mathbf{N}} \mathrm{d}V \tag{3.3a}$$

$$\mathbf{K}_{du} = \int_{\mathcal{B}} \bar{\mathbf{N}}^{\mathrm{T}} \left(\omega' \frac{\partial \mathcal{H}}{\partial \boldsymbol{\epsilon}} \right) \mathbf{B} \mathrm{d}V, \qquad \mathbf{K}_{dd} = \int_{\mathcal{B}} \left[\bar{\mathbf{N}}^{\mathrm{T}} \left(-\frac{\partial Q}{\partial d} \right) \bar{\mathbf{N}} + \frac{2b}{c_\alpha} G_{\mathrm{f}} \bar{\mathbf{B}}^{\mathrm{T}} \bar{\mathbf{B}} \right] \mathrm{d}V \tag{3.3b}$$

Standard Gauss quadrature rules are used to evaluate the above integrals.

It is well-known that the above Newton's monolithic algorithm performs poorly in solving Eq. (2.14) since the underlying energy functional is not convex with respect to both unknowns $\{\mathbf{a}, \bar{\mathbf{a}}\}$; see [4,5] for the details. A few attempts have been proposed in the literature to deal with this issue. For instance, Singh et al. [33] and May et al. [34] suggested using the fracture surface based arc-length method and an adaptive time stepping scheme to enhance the robustness; Gerasimov and De Lorenzis [35] developed a non-conventional line search technique to improve convergence of the monolithic solver; Heister et al. [29] proposed a modified Newton scheme which was later improved in [36] with an adaptive transition from Newton's method to the modified Newton scheme. However, these strategies are not always effective and their applicability to non-standard phase-field damage models, i.e., the AT1 and PF-CZM, needs further investigation.

Remark 3.1. For the unified phase-field damage theory presented in Box I, it follows that

$$\frac{\partial \boldsymbol{\sigma}}{\partial \boldsymbol{\epsilon}} = \omega(d) \mathbb{E}_0, \qquad \frac{\partial \boldsymbol{\sigma}}{\partial d} = \omega'(d) \mathbb{E}_0 : \boldsymbol{\epsilon} \tag{3.4a}$$

$$\frac{\partial \mathcal{H}}{\partial \boldsymbol{\epsilon}} = \begin{cases} \mathbf{0} & \bar{Y}_{n+1} \le \bar{Y}_n \\ \dfrac{\bar{\sigma}_{\mathrm{eq}}}{E_0} \dfrac{\partial \bar{\sigma}_{\mathrm{eq}}}{\partial \boldsymbol{\epsilon}} & \bar{Y}_{n+1} > \bar{Y}_n \end{cases} \tag{3.4b}$$

$$\frac{\partial Q}{\partial d} = -\omega'' \mathcal{H} - \alpha'' \frac{G_{\mathrm{f}}}{c_\alpha b} \tag{3.4c}$$

for the second-order derivatives $\alpha''(d) := \partial \alpha^2 / \partial d^2$ and $\omega''(d) := \partial \omega^2 / \partial d^2$. □

Remark 3.2. Note that the above system of Eqs. (3.2) is not symmetric, i.e., $\mathbf{K}_{ud} \neq \mathbf{K}_{du}$, due to the hybrid formulation and the presence of the history variable $\mathcal{H}$. For mildly nonlinear problems, the off-diagonal matrices can be removed by neglecting the inter-field coupling, leading to

$$\begin{bmatrix} \mathbf{K}_{uu} & \mathbf{0} \\ \mathbf{0} & \mathbf{K}_{dd} \end{bmatrix} \begin{Bmatrix} \delta \mathbf{a} \\ \delta \bar{\mathbf{a}} \end{Bmatrix} = \begin{bmatrix} \mathbf{r} \\ \bar{\mathbf{r}} \end{bmatrix} \tag{3.5}$$

This modified Newton scheme is frequently adopted in solving weakly coupled problems. However, numerical results presented in [36] show that it does not apply to phase-field damage models in which the mechanical responses and damage evolution are strongly coupled. □

3.2. Alternate minimization (staggered) algorithm

Though the underlying energy functional is not convex with respect to (wrt.) both unknowns $(\mathbf{u}, d)$, it is indeed convex wrt. $\mathbf{u}$ and d separately if the other variable is fixed [4,5]. Accordingly, the discrete governing equations (2.14) can be solved by fixing the damage dofs $\bar{\mathbf{a}}$ or the displacement dofs $\mathbf{a}$ alternatingly, resulting in the so-called alternating minimization (AM) or staggered solver. That is, at the kth iteration of a specific time increment $[T_n, T_{n+1}]$, we

- Solve the nodal displacements $\mathbf{a}$ from the mechanical sub-problem with the damage dofs fixed as $\bar{\mathbf{a}}^{(k-1)}$ obtained in the previous iteration, i.e.

$$\mathbf{r} := \mathbf{f}^{\mathrm{ext}} - \int_{\Omega} \mathbf{B}^{\mathrm{T}} \boldsymbol{\sigma} \, \mathrm{d}V = \mathbf{0}, \qquad \boldsymbol{\sigma} = \boldsymbol{\sigma}(\mathbf{a}^{(k)}; \bar{\mathbf{a}}^{(k-1)}) \tag{3.6}$$

  This standard mechanical problem can be solved by the Newton method, with the linearized equation

$$\mathbf{K}_{uu} \delta \mathbf{a} = \mathbf{r} \tag{3.7}$$

  for the stiffness matrix $\mathbf{K}_{uu}$ in Eq. $(3.3a)_1$.

- Solving the nodal unknowns $\bar{\mathbf{a}}$ from the damage sub-problem with the updated nodal displacement $\mathbf{a}^{(k)}$, i.e,

$$\bar{\mathbf{r}} := \int_{\mathcal{B}} \bar{\mathbf{N}}^{\mathrm{T}} Q \mathrm{d}V - \int_{\mathcal{B}} \bar{\mathbf{B}}^{\mathrm{T}} \boldsymbol{q} \, \mathrm{d}V = \mathbf{0}, \qquad Q = Q(\bar{\mathbf{a}}; \mathbf{a}^{(k)}) \tag{3.8}$$

  The linearization form yields

$$\mathbf{K}_{dd} \delta \bar{\mathbf{a}} = \bar{\mathbf{r}} \tag{3.9}$$

  for the stiffness matrix $\mathbf{K}_{dd}$ given in Eq. (3.3b)$_2$.

The above solution procedure is repeated until the final solution converges; see [26] and Wu et al. [2] for more details. Compared to the modified Newton method discussed in Remark 3.2, the crucial difference is that the displacement and damage unknowns are solved alternatingly rather than simultaneously — the former converges but the latter usually does not.

One necessary ingredient of the above AM/staggered solver is the stop or convergence criterion. In the literature, the following options have been considered

- One-pass criterion [12]: In this strategy phase-field models are treated as sequentially coupled damage-mechanical problems. As no overall convergence is checked at each increment, this scheme is very robust and has been widely adopted [50–52]. However, extremely small increments (usually less than $\sim 10^{-5}$) have to be used. Even worse, this scheme may slow down damage evolution, sometimes leading to imprecise or erroneous numerical results.
- Damage-based criterion [4,5,44]: This criterion checks the tolerance of the nodal damage dofs between two consecutive iterations, i.e., $\left|\bar{a}_{n+1}^{(k+1)} - \bar{a}_{n+1}^{(k)}\right| < \epsilon$ for a small positive number, say $\epsilon = 1.0 \times 10^{-5}$, with $|\cdot|$ being an appropriate norm (e.g., L_2-norm). This scheme is also very robust even if large incremental sizes ($\sim 10^{-2}$) are adopted, in particular when it is enhanced with path-following strategies [26].
- Energy-based criterion [1,35]: Similarly to the damage-based criterion, this scheme checks the tolerance of the total energy (1.2), i.e., $\left|\mathscr{E}_{n+1}^{(k+1)} - \mathscr{E}_{n+1}^{(k)}\right| < \epsilon$ between two consecutive iterations. As the total energy is not always sensitive to the solution, very delicate definitions of the energy norm have to be constructed; see [1] for more details.
- Residual-based criterion [35,36,53,54]: In this criterion the residuals $\mathbf{r}$ and $\bar{\mathbf{r}}$ are checked as in the standard FEM. Accordingly, it can be conveniently implemented in commercial software packages.

Though the AM/staggered algorithm is rather robust, the solution converges very slowly. To overcome this issue, Farrell and Maurini [37] interpreted this algorithm as a nonlinear Gauss–Seidel iterative scheme and used an over-relaxed parameter to accelerate the iteration. Once the solution arrives in the convergence basin, the AM algorithm is switched to the Newton monolithic scheme until final solution converges. This composite algorithm was used previously by the author [10,11], but the numerical implementation is not straightforward. Moreover, the transition is usually problem dependent and can only be adjusted in an *ad hoc* manner.

3.3. BFGS quasi-Newton algorithm

The Newton and modified Newton monolithic algorithms perform poorly for phase-field damage models. Comparatively, the AM/staggered solver is robust but it converges very slowly. To reconcile the dilemma between robustness and efficiency, we propose using a quasi-newton monolithic algorithm to solve the coupled governing equations (2.14). In particular, the Broyden–Fletcher–Goldfarb–Shanno (BFGS) method, which can be written in a simple and efficient form for computer implementation, is considered.

In solving the nonlinear equations $\mathbf{g}(\mathbf{z}) = \mathbf{0}$, the quasi-Newton method updates the stiffness matrix $\mathbf{K}$ in a simple manner after each iteration, rather than recalculates it entirely (the Newton method) or leaves it unchanged (the modified Newton method). More specifically, the stiffness matrix $\mathbf{K}$ is replaced by an approximation $\tilde{\mathbf{K}}$ that satisfies the following quasi-Newton equation

$$\tilde{\mathbf{K}}\left(\mathbf{z}^{(k)} - \mathbf{z}^{(k-1)}\right) = \mathbf{g}^{(k)} - \mathbf{g}^{(k-1)} \tag{3.10a}$$

or, equivalently,

$$\tilde{\mathbf{K}} \, \delta \mathbf{z} = \delta \mathbf{g} \tag{3.10b}$$

for the residual $\delta\mathbf{g} := \mathbf{g}^{(k)} - -\mathbf{g}^{(k-1)}$ and the correction $\delta\mathbf{z} := \mathbf{z}^{(k)} - -\mathbf{z}^{(k-1)}$, respectively. The quasi-Newton method is a generalization of the secant method that finds the root of nonlinear equations, introducing new information acquired in the previous increment — the secant in the search direction is made correct. Various quasi-Newton methods differ in how they constrain the solution, typically by adding a simple low-rank update to the current estimate of the stiffness matrix $\tilde{\mathbf{K}}$.

In the BFGS quasi-Newton method, the approximated stiffness $\tilde{\mathbf{K}}$ is updated by a correction matrix of rank 2

$$\tilde{\mathbf{K}} = \tilde{\mathbf{K}}^{(k-1)} - \frac{\left(\mathbf{K}^{(k-1)}\delta\mathbf{z}\right)\left(\mathbf{K}^{(k-1)}\delta\mathbf{z}\right)^{\mathrm{T}}}{\delta\mathbf{z}^{\mathrm{T}}\mathbf{K}^{(k-1)}\delta\mathbf{z}} + \frac{\delta\mathbf{g}\,\delta\mathbf{g}^{\mathrm{T}}}{\delta\mathbf{z}^{\mathrm{T}}\delta\mathbf{g}} \tag{3.11}$$

Moreover, Matthies and Strang [55] have shown that, for systems of equations with a symmetric Jacobian matrix, the BFGS method can be written more conveniently in terms of $\tilde{\mathbf{K}}^{-1}$ rather than $\tilde{\mathbf{K}}$

$$\tilde{\mathbf{K}}^{-1} = \left(\mathbf{I} - \frac{\delta\mathbf{z}\delta\mathbf{g}^{\mathrm{T}}}{\delta\mathbf{z}^{\mathrm{T}}\delta\mathbf{g}}\right)\left(\tilde{\mathbf{K}}^{(k-1)}\right)^{-1}\left(\mathbf{I} - \frac{\delta\mathbf{z}\delta\mathbf{g}^{\mathrm{T}}}{\delta\mathbf{z}^{\mathrm{T}}\delta\mathbf{g}}\right)^{\mathrm{T}} + \frac{\delta\mathbf{z}\,\delta\mathbf{z}^{\mathrm{T}}}{\delta\mathbf{z}^{\mathrm{T}}\delta\mathbf{g}} \tag{3.12}$$

Accordingly, the new search direction can be calculated inexpensively, which is very effective for the computer implementation.

As can be seen, if the initial guess $\tilde{\mathbf{K}}^{(0)}$ is symmetric and positive definite, the updated one $\tilde{\mathbf{K}}$ also is Matthies and Strang [55]. Noticing that the full stiffness matrix (3.2) is not necessarily symmetric and positive-definite, we adopt the uncoupled stiffness matrix (3.5) as the initial guess $\tilde{\mathbf{K}}^{(0)}$

$$\tilde{\mathbf{K}}^{(0)} = \begin{bmatrix} \mathbf{K}_{uu} & \mathbf{0} \\ \mathbf{0} & \mathbf{K}_{dd} \end{bmatrix} \tag{3.13}$$

The mechanical stiffness matrix $\mathbf{K}_{uu}$ is always symmetric and positive-definite. Moreover, the damage stiffness matrix $\mathbf{K}_{dd}$ is always symmetric and its positive definiteness can be guaranteed for an appropriate length scale parameter b; see Remark 3.4. Therefore, the BFGS approximation $\tilde{\mathbf{K}}$ is also symmetric and positive-definite, such that those efficient iterative solvers, e.g., conjugate gradient solver, etc., can be used. Note that, though the initial guess $\tilde{\mathbf{K}}^{(0)}$ is uncoupled, the subsequent approximation is not due to the correction (3.11). This is not the case for the modified Newton method based monolithic algorithm introduced in Remark 3.2.

Practically, the BFGS stiffness matrix $\tilde{\mathbf{K}}$ is formed whenever a specified number (usually 5∼10) of iterations have been done without obtaining a convergent solution, since too many such products are not computationally attractive. In the numerical examples presented later in this work, the default number of iterations is set to 8 above which the stiffness matrix $\tilde{\mathbf{K}}$ is reformed. Note that the quasi-Newton method is slower than the Newton one (if the later converges), but it is much faster than the modified Newton method and the AM/staggered algorithm.

Remark 3.3. The quasi-Newton algorithm works well in combination with the line search method. The later helps to prevent divergence of equilibrium iterations resulting from the inexact stiffness matrix. In this enhanced algorithm, the solution is updated by

$$\mathbf{z}^{(k)} = \mathbf{z}^{(k-1)} + s\delta\mathbf{z} \tag{3.14}$$

where the scaling factor s is chosen such that the residual $\mathbf{g}$ in the search direction is zero (within some tolerance)

$$\delta\mathbf{z}^{\mathrm{T}}\mathbf{g}^{(k)} = 0 \tag{3.15}$$

Practically, the above equation is solved by the Newton method to determine the scaling factor s up to a maximum iteration (usually $N_{\mathrm{ls}} = 5$) or within a specified convergence tolerance (e.g., $\varepsilon = 0.10$). More aggressive line searching can be beneficial for strongly nonlinear problems. In these cases one could use more iterations and more strict tolerance in searching the line scaling factor. This may result in more line search iterations but fewer nonlinear ones, and thus an overall reduction in computational cost. □

Remark 3.4. In order to guarantee the positive-definiteness of the matrix $\mathbf{K}_{dd}$, it is sufficient that

$$-\frac{\partial Q}{\partial d} = \omega''\mathcal{H} + \alpha''\frac{G_{\mathrm{f}}}{c_\alpha b} \geq 0 \tag{3.16}$$

For the phase-field damage models for brittle fracture, e.g., $\omega(d) = \big(1-d\big)^2$ and $\alpha(d) = d^2$ [4,5,12] or $\alpha(d) = d$ [13], the above condition automatically holds. For the PF-CZM with a rational function $\omega(d)$ and $\alpha(d) = 2d - d^2$, the condition (3.16) upon damage nucleation is considered, i.e.,

$$-\frac{\partial Q}{\partial d}\bigg|_{d=0} = \frac{4G_{\mathrm{f}}}{\pi b}\Big(a_1 - a_2 - p - \frac{1}{2}\Big) \geq 0 \qquad \Longrightarrow \qquad b \leq \frac{4}{\big(a_2 + p + \frac{1}{2}\big)\pi} l_{\mathrm{ch}} \tag{3.17}$$

Regarding the linear, exponential and Cornelissen et al. [24] softening laws, it follows that $b \leq \big(0.64 \sim 0.33\big) l_{\mathrm{ch}}$. In practice we can use a length scale parameter $b \leq \frac{1}{3} l_{\mathrm{ch}}$. This is not a limitation since the length scale parameter b has to be sufficiently small to resolve the damage field of highly non-uniform distribution. □

Remark 3.5. As the stiffness matrix (the secant one at fixed damage) $\mathbf{K}_{uu}$ is symmetric, the above BFGS monolithic algorithm also applies to the phase-field anisotropic damage models with positive/negative split [2,12,39]. Moreover, the BFGS monolithic algorithm can also be used together with path-following strategies, e.g., the arc-length method [56], the indirect displacement control [57], as in our previous work [26], in order to enhance the robustness for problems involving snap-backs. Last but not the least, though only quasi-static problems are considered, preliminary results have shown that the BFGS monolithic algorithm also works for dynamic fracture [28,58]. Nevertheless, we do not pursue the above extensions in this work. □

4. Representative numerical examples

In this section several representative numerical examples are presented. Both brittle fracture and quasi-brittle failure are considered by the PF-CZM. The numerical performance of the proposed BFGS monolithic algorithm is compared against that of the AM/staggered solver. Both algorithms are implemented in the commercial FEM software package [59].

In the simulations, the residual-based convergence criterion of ABAQUS is adopted in both algorithms

$$r^z_{\max} \leq \varepsilon_q \tilde{q}^z \tag{4.1}$$

where $r^z_{\max}$ represents the largest residual in the balance equations for the displacement field ($z = u$) or for the damage field ($z = d$), and $\tilde{q}^z$ is an overall time-averaged flux for the displacement and damage achieved so far during this loading step including the current increment. If the condition (4.1) is satisfied for both field variables, convergence is accepted if the following extra criterion is also satisfied

$$c^z_{\max} \leq \varepsilon_c \Delta z_{\max} \tag{4.2}$$

where $c^z_{\max}$ is the largest correction to the field variable z provided by the current iteration and $\Delta z_{\max}$ is the largest incremental change to the corresponding solution variable in the current load increment. The default tolerances $\varepsilon_q = 0.005$ and $\varepsilon_c = 0.01$ are used.

Fortunately, the BFGS algorithm has already been incorporated in ABAQUS and can be simply activated by the following keyword

```
*SOLUTION TECHNIQUE, TYPE=QUASI-NEWTON
```

In this case, the line search strategy is activated by default with $N_{\mathrm{ls}} = 5$ for the BFGS quasi-Newton method. As strong nonlinearities are usually involved in cracks propagation, the number of iterations may become excessive. The default control on iterations in ABAQUS is too stringent and would decrease the incremental size frequently. In order to overcome this issue, one can specify a number of time incrementation control parameters (see the keyword manual of ABAQUS [59] for the details), e.g.,

```
*CONTROLS, PARAMETERS=TIME INCREMENTATION
 5000, 5000, , 5000, 5000, , , 10, , ,
```

As will be seen, it is not unusual that the AM/stagger algorithm needs more than 1000 iterations for some critical increments.

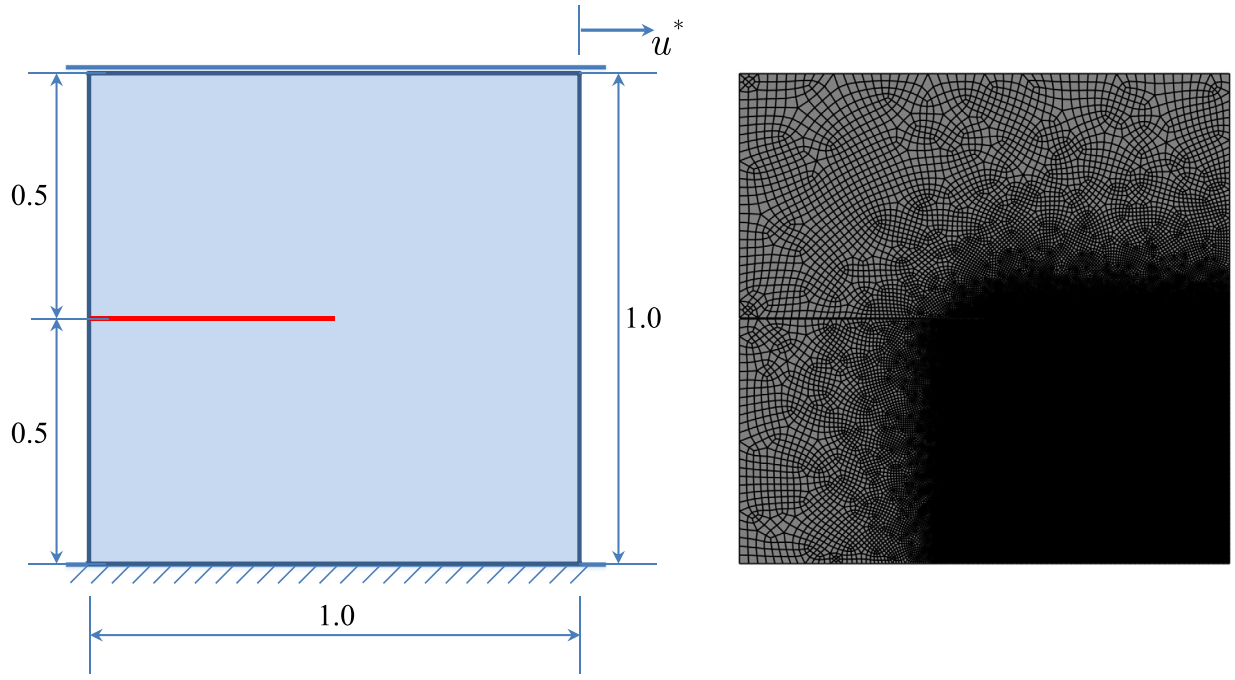

(a) Geometry (unit of length: mm), boundary and loading conditions (b) Finite element discretization (about 390,000 elements)

Fig. 2. Single-edge notched plate: problem setting and finite element discretization.

Plane stress is assumed in all simulations. The Rankine definition $(2.1)_1$ is considered unless otherwise specified explicitly. Quadrilateral bilinear elements (Q4) are used to discretize the computational domain. Provided the damage sub-domain can be properly selected *a priori*, it is discretized by fine mesh with size $h \leq \frac{1}{5}b$ while the remaining one by coarse mesh with larger size, respectively; otherwise, uniform mesh size $h \leq \frac{1}{5}b$ is used in the whole computational domain. Predefined cracks, if exist, are modeled straightforwardly by geometry and mesh discretization. As it has been extensively verified that for both brittle fracture and quasi-brittle failure the PF-CZM is sensitive neither to the length scale parameter nor to the mesh size/alignment [2,10,11,22,25–27,42], in each example only a single set of length scale parameter $b \leq \frac{1}{3}l_{\text{ch}}$ and mesh size $h \leq \frac{1}{5}b$ are adopted. All the simulations were run on a workstation with Intel(R) Core(TM) i7-7700HQ CPU @ 2.80 GHz and 32 GB RAM.

Remark 4.1. By simply removing the keyword `*SOLUTION TECHNIQUE, TYPE=QUASI-NEWTON`, the modified Newton monolithic algorithm mentioned previously in Remark 3.2 is recovered from the BFGS algorithm implemented in ABAQUS. As will be seen from Section 4.2, this algorithm is much slower than the BFGS one even if it converges sometimes. □

4.1. Single-edge notched plate subjected to shear loading (SENP-shear)

Let us first consider a single edge-notched plate subjected to shear loading. As shown in Fig. 2(a), it is a square plate of length 1 mm, with unit out-of-plane thickness. A straight horizontal notch of length 0.5 mm is introduced at the mid-height of the left edge. The plate is fixed at the bottom edge and applied by a horizontal displacement at the top edge. Being a popular benchmark in verifying phase-field damage models for brittle fracture [1,12,22], this example is very challenging to the numerical algorithm used to solve the governing equations; see [29], [35] and [36] for the discussion on `AT2` for brittle fracture.

The following material parameters are adopted: Young's modulus $E_0 = 2.1 \times 10^5$ MPa, Poisson's ratio $\nu_0 = 0.3$, the failure strength $f_t = 2000$ MPa and the fracture toughness $G_{\text{f}} = 2.7$ N/mm, resulting in an Irwin's length

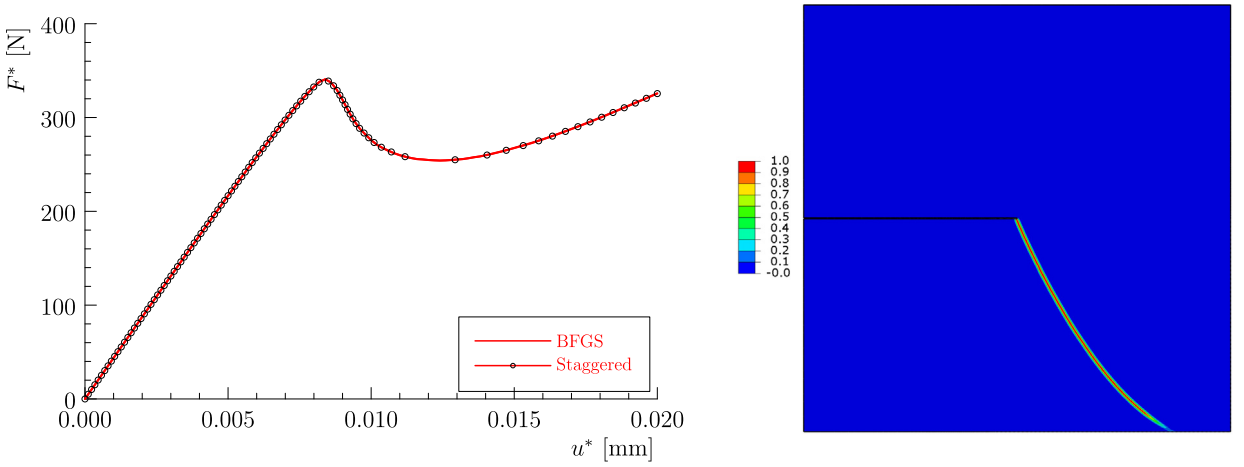

(a) Load *versus* displacement curves

(b) Damage profile at $u^* = 0.02$ mm

Fig. 3. Single-edge notched plate: Global responses and damage profile.

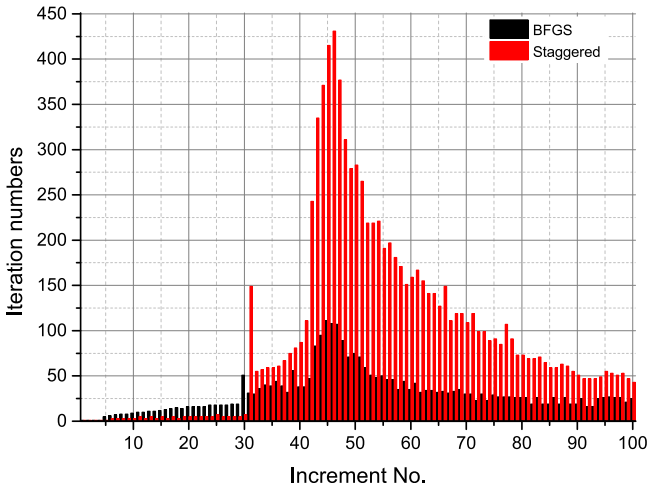

Fig. 4. Single-edge notched plate: Iteration numbers at each increment.

$l_{\text{ch}} = 0.14$ mm. In accordance with Wu and Nguyen [22], the linear softening law is assumed for brittle fracture. The length scale parameter $b = 0.005$ mm is considered, with the mesh size $h = 0.001$ mm within the damage sub-domain *a priori* selected as in Fig. 2(b). The prescribed displacement $u^* = 0.02$ mm is applied in 100 equal increments, i.e., $\Delta u^* = 2.0 \times 10^{-4}$ mm.

Fig. 3(a) depicts the load *versus* displacement curves given by the AM/staggered solver and the presented BFGS monolithic algorithm. As can be seen, the global responses are not affected by the adopted solution schemes. This is a favorable hope that a numerical algorithm in general should not change the physical results, which is indeed the case here. The predicted damage profile at the applied displacement $u^* = 0.02$ mm is shown in Fig. 3(b). As the results given by both algorithms coincide, only one of them is presented. The above global response and damage profile also coincide with those given in [22] that adopted the AM/staggered solver with the damage-based criterion.

Though the AM/staggered solver and the presented BFGS monolithic algorithm give identical numerical results, their performances are remarkably different. Fig. 4 presents the iteration numbers at each increment. As can be seen, for the staggered solver a total of 9374 iterations are needed to complete the analysis and more than 30 increments need over 100 iterations to converge. In particular, the critical increments, INC. 45 and INC. 46, in which crack

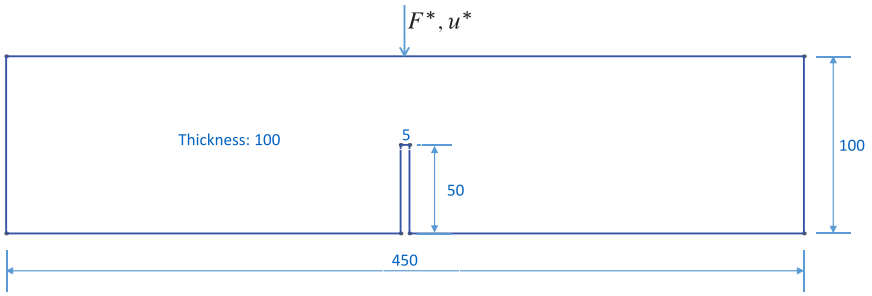

Fig. 5. Notched concrete beam under mode-I failure: Geometry (unit of length: mm), loading and boundary conditions.

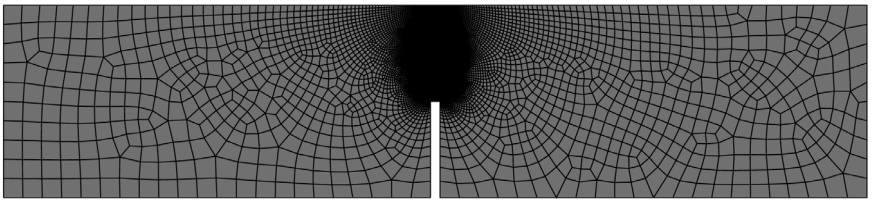

Fig. 6. Notched concrete beam under mode-I failure: Finite element mesh (about 20,000 Q4 elements).

propagates rapidly through the plate, need more than 400 iterations. Comparatively, the presented BFGS monolithic algorithm needs a total of 3131 iteration, about one third of that for the staggered solver, to complete the analysis. Moreover, almost all the increments converge within 100 iterations, and even at the most critical increment, INC. 45, only 114 iterations are needed for convergence. Compared to the AM/staggered solver, the above numerical performance is rather satisfactory for this challenging issue.

The saving in computational cost is even more pronounced. The total CPU times are 60 780 s for the BFGS monolithic algorithm *versus* 417 600 s for the staggered solver, the former being about 6.87 times faster than the later. This acceleration is due to less iterations and less reformations of the stiffness matrix per increment.

4.2. Notched concrete beam under mode-I failure (3pt-bending)

A notched beam under three-point bending reported in [60] is then considered. The specimen was made of concrete, a typical quasi-brittle material, with the geometric, loading and boundary conditions shown in Fig. 5. As expected, in the test the beam failed due to a crack emerging from the notch tip and propagating vertically along the line of symmetry.

The material properties are taken from Rots [60]: $E_0 = 2.0 \times 10^4$ MPa, $\nu_0 = 0.2$, $f_t = 2.4$ MPa and $G_{\mathrm{f}} = 0.113$ N/mm, resulting in an Irwin's length $l_{\mathrm{ch}} = 392.4$ mm. The Cornelissen et al. [24] softening curve is assumed for concrete. The length scale parameter $b = 2.5$ mm is adopted, with the mesh size $h = 0.25$ mm around centroid of the beam as shown in Fig. 6. The prescribed displacement $u^* = 1$ mm is applied in 100 equal increments, i.e., $\Delta u^* = 0.01$ mm.

Fig. 7 depicts the load *versus* deflection curves. As expected, the AM/staggered solver and the presented BFGS monolithic algorithm give identical results and the global responses are not affected by the adopted solution schemes. This conclusion is further confirmed from the damage profile at the deflection $u^* = 1$ mm shown in Fig. 8 (in order to avoid duplication, only one of them is presented). As can be seen, a crack nucleates at the notch tip and propagates upward to the beam top.

Though both algorithms give identical numerical results, their performances differ significantly. Fig. 9 presents the iteration numbers at each increment. Compared to the BFGS monolithic algorithm, the AM/staggered solver needs about twice iterations (4046 *versus* 2073) to complete the analysis. Moreover, there are much more (17 *versus* 3) increments that need over 50 iterations. In particular, at the critical increment, INC. 5, the AM/staggered solver needs 387 iterations to converge. Comparatively, the BFGS monolithic algorithm performs much better and

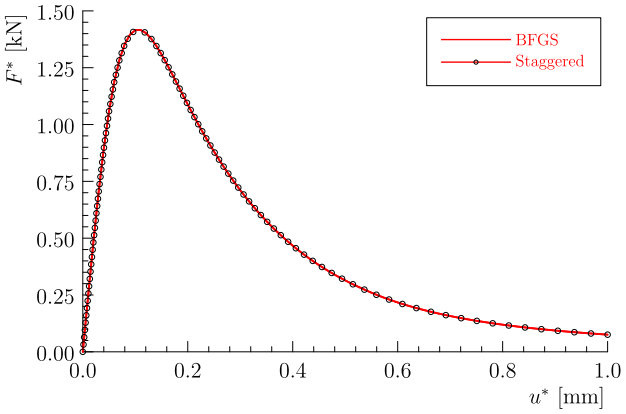

Fig. 7. Notched concrete beam under mode-I failure: Load *versus* deflection curves.

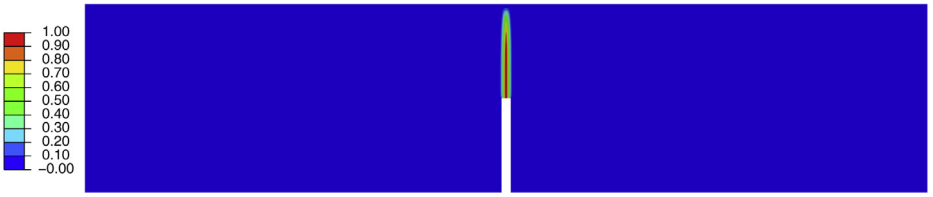

Fig. 8. Notched concrete beam under mode-I failure: Damage profile at u^*.

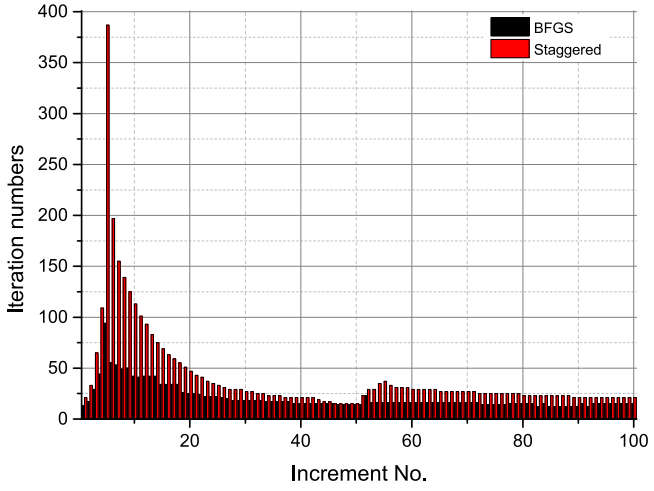

Fig. 9. Notched concrete beam under mode-I failure: Iteration numbers at each increment.

converges within 50 iterations for almost all the increments. Even at the most critical INC. 5, only 94 iterations are needed for convergence, which is acceptable in the context of phase-field damage models.

Regarding the CPU times, they are about 1980 s for the BFGS monolithic algorithm *versus* 5640 s for the staggered solver. Even for this relative simple example, the BFGS monolithic algorithm have achieved considerable saving in computational cost (about 2.76 times).

Remark 4.2. For this simple example, the modified Newton method based monolithic algorithm introduced in Remark 3.2 also works. The total iteration number is 3475 and the CPU time is 4900 s, which are comparable to

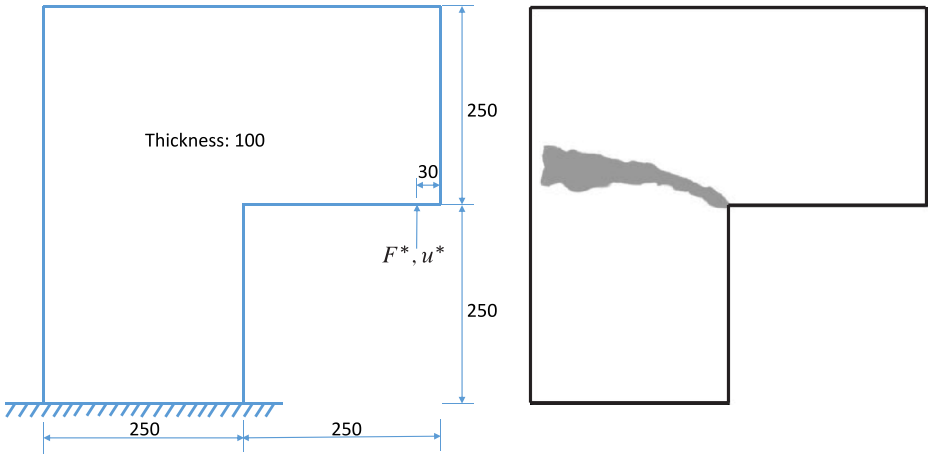

Fig. 10. L-shaped panel [61]: Geometry (unit of length: mm), loading and boundary conditions (left); Experimental observed crack path (right).

those of the AM/staggered solver. However, as illustrated in [36], the modified Newton method based monolithic algorithm does not always work for brittle fracture involving abrupt crack propagation. □

4.3. L-shaped panel under mixed-mode failure (L-shaped)

The L-shaped panel conducted by Winkler [61] is a well-known benchmark test of concrete under mixed-mode failure [10,11,62–64]. The geometry, loading and boundary conditions of the specimen are shown in Fig. 10. The bottom edge of the specimen is fixed. A vertical point load F^* is applied upward at a distance of 30 mm to the right edge of the horizontal leg, with the corresponding vertical displacement u^* at the same place recorded.

The material properties are taken from Unger et al. [63]: $E_0 = 2.0 \times 10^4$ MPa, $\nu_0 = 0.18$, $f_t = 2.5$ MPa and $G_f = 130$ J/m^2, resulting in an Irwin's length $l_{ch} = 416$ mm. The length scale parameter $b = 5.0$ mm is adopted, with the mesh size $h = 1.0$ mm within the damage sub-domain as shown in Fig. 11(a). The prescribed displacement $u^* = 1$ mm is applied in 50 equal increments, resulting in a large incremental size $\Delta u^* = 0.02$ mm.

Fig. 11(b) shows the damage profile at $u^* = 1$ mm. As the results given by the AM/staggered solver and the BFGS algorithms are identical, here only one of them is presented. Similarly to our previous results given by the AM/staggered solver with damage-based criterion, the predicted crack path agrees well with the experimentally observed range. Again, the numerical prediction is independent of the adopted algorithm as expected; see the load *versus* displacement curves shown in Fig. 12.

The numerical performances of both algorithms are compared in Fig. 13. For this example involving large incremental size, the AM/staggered solver needs a total of 4444 iterations to complete the analysis. Moreover, 16 among the prescribed 50 increments demand iterations larger than 100. In particular, at the critical increments, INC. 9 and INC. 10, the iteration numbers exceed 300. Comparatively, the BFGS monolithic algorithm needs only 1901 iterations to complete the simulation. The most critical increments (INC. 9 and INC. 10) need only 108 iterations. The corresponding CPU time is 1860 s, about 4.4 times faster than that of the AM/staggered solver (8160 s).

4.4. Double edge-notched specimen under mixed failure (DENS-4b)

Finally, let us consider the double-edge notched specimen (DENS) test reported in [65], limited to the so-called DENS-4b (46-05). As shown in Fig. 14(a), it is a plain concrete specimen of dimensions 200 × 200 × 50 mm^3, with two notches of sizes 25 × 5 × 50 mm^3 at the center of left and right hand sides. The specimen was glued to a special rigid steel frame. More specifically, the specimen, supported at the bottom and the right-hand side below the notch, was first subjected to a horizontal "shear" force $F_s^* = 10$ kN along the left hand side above the notch, and then a vertical normal force F^* was applied at the top with monotonically increasing displacement u^* while

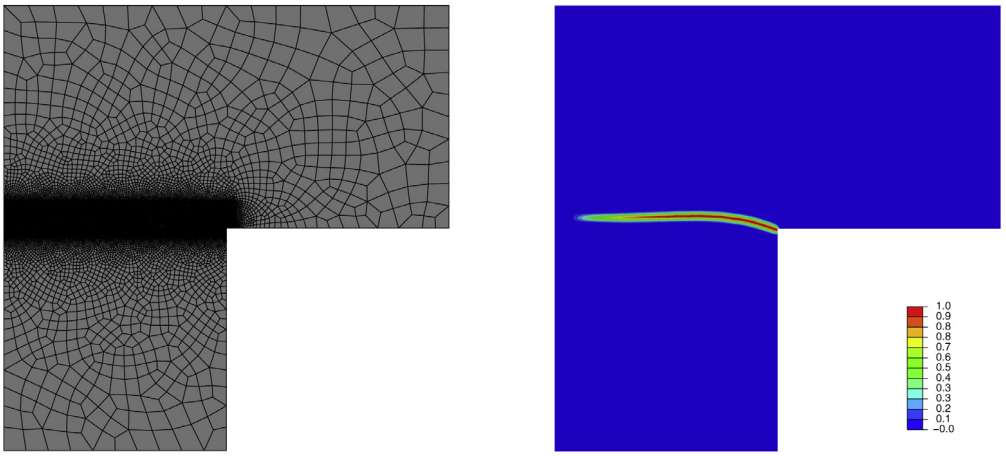

(a) Finite element discretization (b) Damage profile at $u^* = 1$ mm

Fig. 11. L-shaped panel: Finite element mesh (about 20,000 Q4 elements) and damage profile.

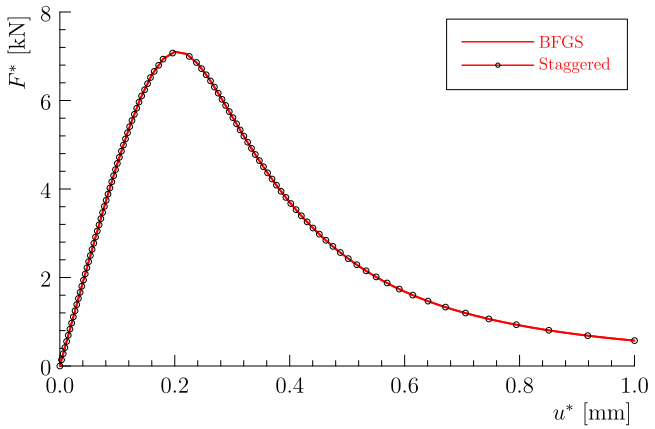

Fig. 12. L-shaped panel: Numerically predicted load *versus* displacement curves.

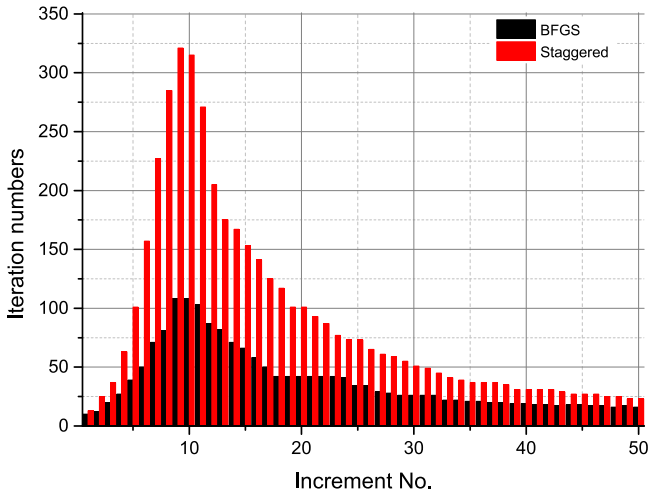

Fig. 13. L-shaped panel [61]: Comparison of iteration numbers at each increment.

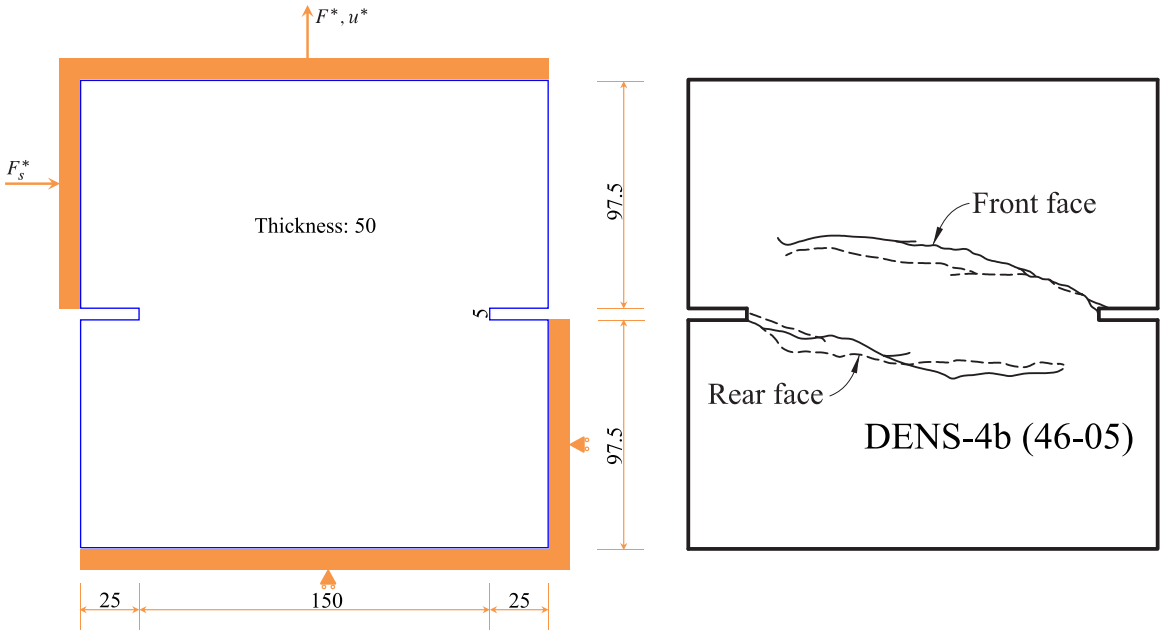

(a) Geometry (unit: mm), boundary conditions and loading

(b) Experimentally observed cracks

Fig. 14. Double edge notched specimen [65]: Experimental test.

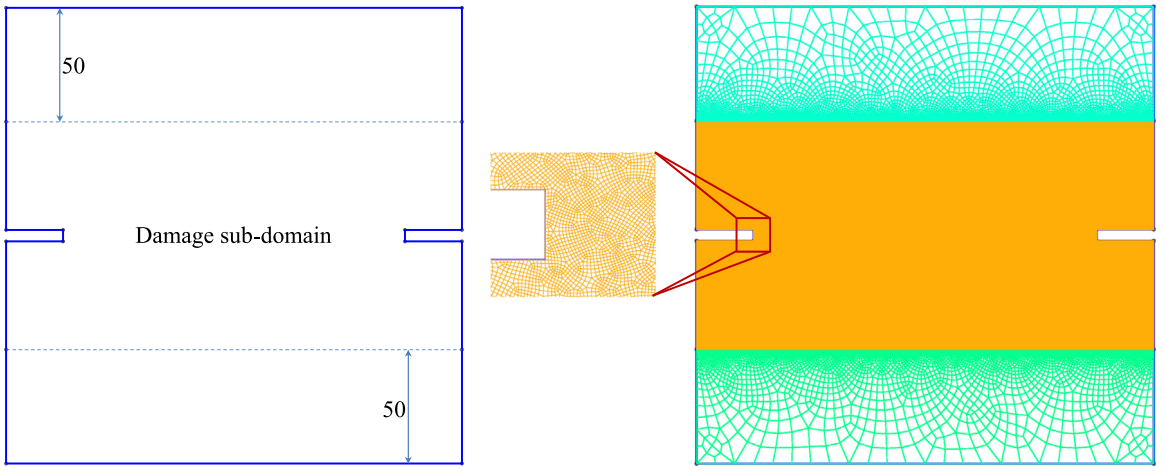

(a) Refined damage sub-domain and coarse elastic one

(b) Finite element mesh (about 230,000 Q4 elements)

Fig. 15. Double edge notched specimen: Mesh strategy adopted in the simulations.

the shear force F_s^* was maintained constantly. Two nearly antisymmetric cracks propagating from the notches to the opposite sides were experimentally observed; see Fig. 14(b).

Though not necessarily, a damage sub-domain is selected *a priori* as shown in Fig. 15(a) and discretized into refined uniform Q4 elements with mesh size $h = 0.3$ mm. The horizontal shear load F_s^* is applied by force control equally in 10 increments and the vertical normal load F^* by imposing increasing displacements u^*. The total vertical displacement $u^* = 0.20$ mm is applied equally in 100 incremental steps. The rigid frame is modeled by linear constraints such that the horizontal displacements of those nodes on the left upper edge are equal, and so are

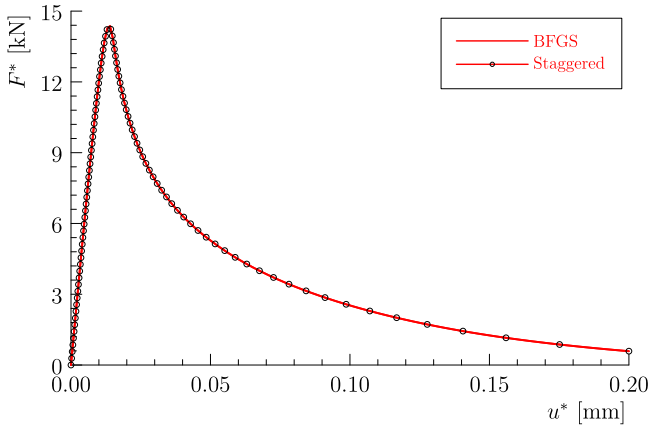

Fig. 16. Double edge notched specimen: Numerically predicted load *versus* displacement curves.

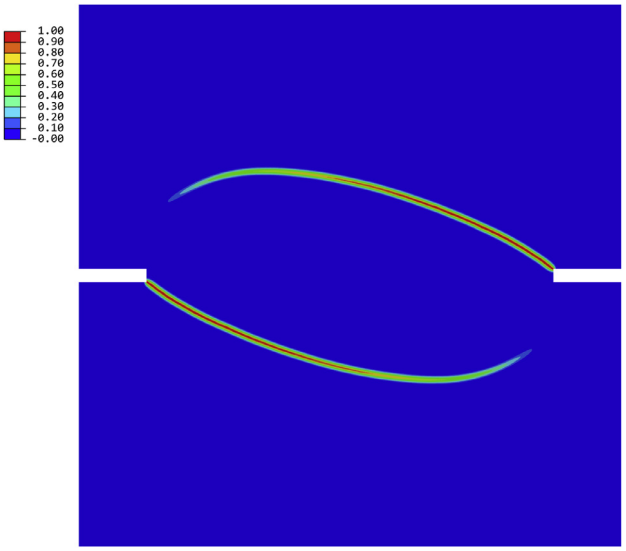

Fig. 17. Double edge notched specimen: Numerically predicted crack patterns at $u^* = 0.2$ mm.

the vertical displacements of those nodes on the top edge. The nodes on the bottom edge are vertically constrained, whereas those on the right lower edge are horizontally constrained.

The material properties are taken from Dumstorff and Meschke [62] and Zhang et al. [66], i.e., Young's modulus $E_0 = 3.0 \times 10^4$ MPa, Poisson's ratio $\nu_0 = 0.2$, the tensile strength $f_t = 3.0$ MPa and the fracture energy $G_{\mathrm{f}} = 0.11$ N/mm, together with the modified von Mises damage criterion $(2.1)_2$ and the Cornelissen et al. [24] softening law. The resulting Irwin's characteristic length is $l_{\mathrm{ch}} = 367$ mm. The length scale parameter $b = 5$ h $= 1.5$ mm is adopted, such that the damage gradient can be sufficiently resolved.

The numerically predicted load *versus* displacement curves given by both solvers are compared in Fig. 16. As expected, the numerical algorithm does not change the global response. Similarly, the predicted damage profiles are not affected, either, and so only that given by the BFGS algorithm, is presented in Fig. 17.

The numerical performances of both algorithms are compared in Fig. 18. For this challenging example with multiple cracks propagating simultaneously, the AM/staggered solver needs a total of 11 340 iterations to complete the analysis. Moreover, 13 among the prescribed 110 increments need iterations larger than 200. In particular, at the critical increments, INC. 25 and INC. 26, the iteration numbers even exceed 1200. Comparatively, the BFGS monolithic algorithm needs only 3784 iterations to complete the simulation. Even for the most critical increments

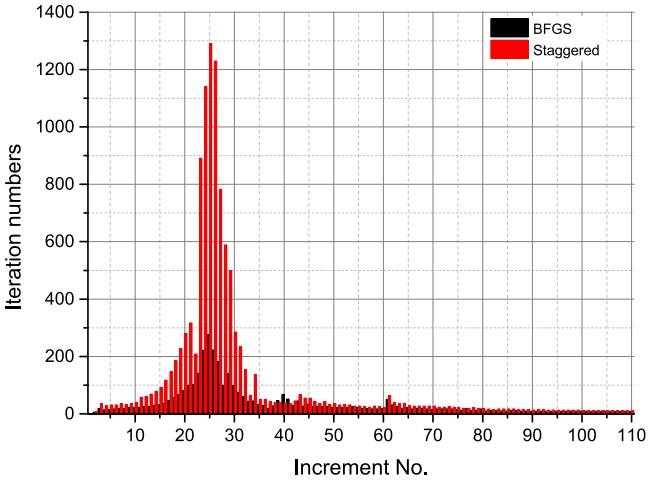

Fig. 18. Double edge notched specimen: Comparison of iteration numbers at each increment.

Table 1
Comparison between the computational performances of the alternate minimization (AM) and BFGS monolithic solvers

Examples	Failure mode	Element No.	Inc. size	Total iter. No.	Max. iter. No.	CPU time (s)
SENP-shear	brittle mixed-mode	∼390 000	0.01	9374 (AM) 3131 (BFGS)	431 (AM) 111 (BFGS)	417 600 (AM) 0780 (BFGS)
3pt-bending	quasi-brittle mode-I	∼20 000	0.01	4046 (AM) 2073 (BFGS)	387 (AM) 94 (BFGS)	5640 (AM) 1980 (BFGS)
L-shaped	quasi-brittle mode-I	∼20 000	0.02	4444 (AM) 1860 (BFGS)	321 (AM) 108 (BFGS)	8160 (AM) 1860 (BFGS)
DENS-4b	quasi-brittle mode-I	∼230 000	0.01	11 430 (AM) 3784 (BFGS)	1291 (AM) 277 (BFGS)	206 820 (AM) 20 220 (BFGS)

the iteration numbers are less than 300. The corresponding CPU time is 50 220 s, about 4.1 times faster than that of the AM/staggered solver (206 820 s).

4.5. Discussion on the computational efficiency

Regarding the above numerical examples, the details are summarized in Table 1.

Note again that the numerical implementations of both the BFGS algorithm and the AM/staggered solver are based upon the same platform — ABAQUS, using the same programming environment and same convergence criteria. Furthermore, the comparison was made with respect to those representative benchmark examples in the phase-field community, and both brittle and quasi-brittle failure in either mode-I and mixed-mode are considered. From the iteration numbers and CPU times reported from all examples, it can be drawn that the gains in computational efficiency are about ∼3 (2.76) times for the smallest problem and ∼7 (6.87) for the largest one.

5. Conclusions

Aiming to improve the computational efficiency of phase-field damage models, in this work we have presented a quasi-Newton monolithic algorithm for solving the coupled governing equations. This Broyden–Fletcher–Goldfarb–Shanno (BFGS) algorithm is, at least the same robust as, but much more efficient than, the popular alternating minimization (AM) or staggered solver. The robustness comes from the BFGS algorithm with a symmetric and positive-definite system matrix, while the efficiency results from the fact that much less iterations and reformulations of the system matrix per increment are needed.

Representative benchmark examples shown that the proposed BFGS algorithm applies to both brittle fracture and quasi-brittle failure with a single or multiple cracks. It is about 3∼7 times faster than the AM/staggered solver, and

the larger the problem is, the more saving it gains in the computational cost. Moreover, the numerical implementation is straightforward since the BFGS algorithm has been widely incorporated in open-source and commercial solvers.

With the significant improvement of computational efficiency, it is possible to apply the `PF-CZM` and other phase-field damage models to more practical and complex 3D problems. Moreover, the proposed BFGS monolithic algorithm can also be used for gradient-enhanced damage models [67–69] and multi-physical phase-field models [70] that share the similar coupled governing equations. These topics will be addressed in forthcoming jobs.

Acknowledgments

The support from the National Natural Science Foundation of China (51678246; 51878294), the State Key Laboratory of Subtropical Building Science, China (2018ZC04) and the Funding for Central Universities, China (2018PY20) to the first author (J.Y. Wu) is acknowledged. The third author (V.P. Nguyen) thanks the funding support from the Australian Research Council via DECRA project DE160100577.

References

[1] M. Ambati, T. Gerasimov, L. de Lorenzis, A review on phase-field models for brittle fracture and a new fast hybrid formulation, Comput. Mech. 55 (2015) 383–405.
[2] J.Y. Wu, V.P. Nguyen, C.T. Nguyen, D. Sutula, S. Sinaie, S. Bordas, Phase Field Modeling of Fracture, in: Advances in Applied Mechancis: Fracture Mechanics: Recent Developments and Trends volume, vol. 53, 2019, in press.
[3] G. Francfort, J. Marigo, Revisting brittle fracture as an energy minimization problem, J. Mech. Phys. Solids 46 (8) (1998) 1319–1342.
[4] B. Bourdin, G. Francfort, J.-J. Marigo, Numerical experiments in revisited brittle fracture, J. Mech. Phys. Solids 48 (4) (2000) 797–826.
[5] B. Bourdin, G. Francfort, J.-J. Marigo, The variational approach to fracture, Springer, Berlin, 2008.
[6] L. Ambrosio, V.M. Tortorelli, Approximation of functional depending on jumps by elliptic functional via t-convergence, Comm. Pure Appl. Math. 43 (8) (1990) 999–1036.
[7] I.S. Aranson, V.A. Kalatsky, V.M. Vinokur, Continuum field description of crack propagation, Phys. Rev. Lett. 85 (2000) 118–121.
[8] A. Karma, D. Kessler, H. Levine, Phase-field model of mode III dynamic fracture, Phys. Rev. Lett. 87 (2001) 118–121.
[9] R. Spatschek, E. Brener, A. Karma, Phase field modeling of crack propagation, Phil. Mag. 9 (2011) 75–95.
[10] J.Y. Wu, A unified phase-field theory for the mechanics of damage and quasi-brittle failure in solids, J. Mech. Phys. Solids 103 (2017) 72–99.
[11] J.Y. Wu, A geometrically regularized gradient-damage model with energetic equivalence, Comput. Methods Appl. Mech. Engrg. 328 (2018a) 612–637.
[12] C. Miehe, M. Hofacker, F. Welschinger, A phase field model for rate-independent crack propagation: Robust algorithmic implementation based on operator splits, Comput. Methods Appl. Mech. Engrg. 199 (45–48) (2010) 2765–2778.
[13] K. Pham, H. Amor, J.-J. Marigo, C. Maurini, Gradient damage models and their use to approximate brittle fracture, Int. J. Damage Mech. 20 (2011) 618–652.
[14] C. Kuhn, A. Schlüter, R. Müller, On degradation functions in phase field fracture models, Comput. Mater. Sci. 108 (2015) 374–384.
[15] M.J. Borden, T.J. Hughes, C.M. Landis, A. Anvari, I.J. Lee, A phase-field formulation for fracture in ductile materials: Finite deformation balance law derivation, plastic degradation, and stress triaxiality effects, Comput. Methods Appl. Mech. Engrg. 312 (2016) 130–166.
[16] C.V. Verhoosel, R. de Borst, A phase-field model for cohesive fracture, Internat. J. Numer. Methods Engrg. 96 (2013) 43–62.
[17] J. Vignollet, S. May, R. de Borst, C.V. Verhoosel, Phase-field model for brittle and cohesive fracture, Meccanica 49 (2014) 2587–2601.
[18] S. May, J. Vignollet, R. de Borst, A numerical assessment of phase-field models for brittle and cohesive fracture: G-convergence and stress oscillations, Eur. J. Mech. A Solids 52 (2015) 72–84.
[19] T.T. Nguyen, J. Yvonnet, Q.-Z. Zhu, M. Bornert, C. Chateau, A phase-field method for computational modeling of interfacial damage interacting with crack propagation in realistic microstructures obtained by microtomography, Comput. Methods Appl. Mech. Engrg. 312 (2016) 567–595.
[20] S. Conti, M. Focardi, F. Iurlano, Phase field approximation of cohesive fracture models, Ann. Inst. Henri Poincare C Non Linear Anal. 33 (4) (2015) 1033–1067.
[21] M. Focardi, F. Iurlano, Numerical insight of a variational smeared approach to cohesive fracture, J. Mech. Phys. Solids 98 (2017) 156–171.
[22] J.Y. Wu, V.P. Nguyen, A length scale insensitive phase-field damage model for brittle fracture, J. Mech. Phys. Solids 119 (2018) 20–42.
[23] G.I. Barenblatt, The formation of equilibrium cracks during brittle fracture. general ideas and hypotheses. axially-symmetric cracks, J. Appl. Math. Mech. 23 (1959) 622–636.
[24] H. Cornelissen, D. Hordijk, H. Reinhardt, Experimental determination of crack softening characteristics of normalweight and lightweight concrete, Heron 31 (2) (1986) 45–56.
[25] T.K. Mandal, V.P. Nguyen, J.Y. Wu, Length scale and mesh bias sensitivity of phase-field models for brittle and cohesive fracture, Eng. Fract. Mech. 217 (2019) 106532.
[26] J.Y. Wu, Numerical implementation of non-standard phase-field damage models, Comput. Methods Appl. Mech. Engrg. 340 (2018b) 767–797.

[27] J.Y. Wu, J.F. Qiu, V.P. Nguyen, L.J. Zhuang, K.M. Tushar, Computational modeling of localized failure in solids: XFEM vs PF-CZM, Comput. Methods Appl. Mech. Engrg. 345 (2019) 618–643.
[28] V.P. Nguyen, J.Y. Wu, Modeling dynamic fracture of solids using a phase-field regularized cohesive zone model, Comput. Methods Appl. Mech. Engrg. 340 (2018) 1000–1022.
[29] T. Heister, M.F. Wheeler, T. Wick, A primal-dual active set method and predictor-corrector mesh adaptivity for computing fracture propagation using a phase-field approach, Comput. Methods Appl. Mech. Engrg. 290 (2015) 466–495.
[30] M. Artina, M. Fornasier, S. Micheletti, S. Perotto, Anisotropic mesh adaptation for crack detection in brittle materials, SIAM J. Sci. Comput. 37 (4) (2015) B633–B659.
[31] N. Ferro, S. Micheletti, S. Perotto, Anisotropic mesh adaptation for crack propagation induced by a thermal shock in 2D, Comput. Methods Appl. Mech. Engrg. 331 (2018) 138–158.
[32] S. Micheletti, S. Perotto, M. Signorini, Anisotropic mesh adaptation for the generalized Ambrosio–Tortorelli functional with application to brittle fracture, Comput. Math. Appl. 75 (6) (2018) 2134–2152.
[33] N. Singh, C. Verhoosel, R. de Borst, E. van Brummelen, A fracture-controlled path-following techniques for phase-field modeling of brittle fracture, Finite Elem. Anal. Des. 113 (2015) 14–29.
[34] S. May, J. Vignollet, R. de Borst, A new arc-length control method based on the rates of the internal and the dissipated energy, Eng. Comput. 33 (1) (2016) 100–115.
[35] T. Gerasimov, L. De Lorenzis, A line search assisted monolithic approach for phase-field computing of brittle fracture, Comput. Methods Appl. Mech. Engrg. 312 (2016) 276–303.
[36] T. Wick, Modified Newton methods for solving fully monolithic phase-field quasi-static brittle fracture propagation, Comput. Methods Appl. Mech. Engrg. 325 (2017) 577–611.
[37] P. Farrell, C. Maurini, Linear and nonlinear solvers for variational phase-field models of brittle fracture, Internat. J. Numer. Methods Engrg. 109 (5) (2017) 648–667.
[38] H.L. Ren, X.Y. Zhuang, C. Anitescu, T. Rabczuk, An explicit phase field method for brittle dynamic fracture, Comput. Struct. 217 (2019) 45–56.
[39] J.Y. Wu, V.P. Nguyen, H. Zhou, Y. Huang, A variationally consistent phase-field anisotropic damage model for fracture, Comput. Methods Appl. Mech. Engrg. (2019b) 358: 112629.
[40] T.K. Mandal, V.P. Nguyen, A. Heidarpour, Phase field and gradient enhanced damage models for quasi-brittle failure: A numerical comparative study, Eng. Fract. Mech. 207 (2019) 48–67.
[41] E. Tanné, T. Li, B. Bourdin, J.-J. Marigo, C. Maurini, Crack nucleation in variational phase-field models of brittle fracture, J. Mech. Phys. Solids 110 (2018) 80–99.
[42] D.C. Feng, J.Y. Wu, Phase-field regularized cohesize zone model (CZM) and size effect of concrete, Eng. Fract. Mech. 197 (2018) 66–79.
[43] S.J. Benson, T.S. Munson, Flexible complementarity solvers for large-scale applications, Optim. Methods Softw. 21 (2006) 155–168.
[44] H. Amor, J. Marigo, C. Maurini, Regularized formulation of the variational brittle fracture with unilateral contact: numerical experiments, J. Mech. Phys. Solids 57 (2009) 1209–1229.
[45] M.F. Wheeler, T. Wick, W. Wollner, An augmented-Lagrangian method for the phase-field approach for pressurized fractures, Comput. Methods Appl. Mech. Engrg. 271 (2014) 69–85.
[46] T. Gerasimov, L. De Lorenzis, On penalization in variational phase-field models of brittle fracture, Comput. Methods Appl. Mech. Engrg. 354 (2019) 990–1026.
[47] E. Lorentz, V. Godard, Gradient damage models: Towards full-scale computations, Comput. Methods Appl. Mech. Engrg. 200 (2011) 1927–1944.
[48] T. Li, J.-J. Marigo, D. Guilbaud, S. Potapov, Gradient damage modeling of brittle fracture in an explicit dynamics context, Internat. J. Numer. Methods Engrg. 108 (11) (2016) 1381–1405.
[49] T. Hughes, The Finite Element Method. Linear Static and Dynamic Finite Element Analysis, Dover Publications Inc., Mineaola, New York, 2000.
[50] M.A. Msekh, J.M. Sargado, M. Jamshidian, P.M. Areias, T. Rabczuk, Abaqus implementation of phase-field model for brittle fracture, Comput. Mater. Sci. 96, Part B (2015) 472–484.
[51] G. Liu, Q. Li, M.A. Msekh, Z. Zuo, Abaqus implementation of monolithic and staggered schemes for quasi-static and dynamic fracture phase-field model, Comput. Mater. Sci. 121 (2016) 35–47.
[52] G. Molnár, A. Gravouil, 2D and 3D abaqus implementation of a robust staggered phase-field solution for modeling brittle fracture, Finite Elem. Anal. Des. 130 (2017) 27–38.
[53] P. Zhang, X. Hu, X. Wang, W. Yao, An iteration scheme for phase field model for cohesive fracture and its implementation in abaqus, Eng. Fract. Mech. 204 (2018) 268–287.
[54] K. Seleš, T. Lesičar, Z. Tonković, J. Sorić, A residual control staggered solution scheme for the phase-field modeling of brittle fracture, Eng. Fract. Mech. 205 (2019) 370–386.
[55] H. Matthies, G. Strang, The solution of nonlinear finite element equations, Internat. J. Numer. Methods Engrg. 14 (1979) 1613–1626.
[56] E. Riks, An incremental approach to the solution of snapping and buckling problems, Int. J. Solids Struct. 15 (7) (1979) 529–551.
[57] R. de Borst, Computation of post-bifurcation and post-failure behavior of strain-softening solids, Comput. Struct. 25 (1987) 211–224.
[58] Z. Wang, A. Shedbale, S. Kumar, L.H. Poh, Localizing gradient damage model with micro inertia effect for dynamic fracture, Comput. Methods Appl. Mech. Engrg. 355 (2019) 492–512.
[59] I. ABAQUS, ABAQUS 6.3 Analysis User's Manual, 2002.
[60] J. Rots, Computational Modeling of Concrete Fracture (Ph.D. thesis), Delft University of Technology, Netherlands., 1988.

[61] B. Winkler, Traglastuntersuchungen von unbewehrten und bewehrten Betonstrukturen auf der Grundlage eines objektiven Werkstoffgesetzes für Beton (Ph.D. thesis), Universität Innsbruck, Austria, 2001.
[62] P. Dumstorff, G. Meschke, Crack propagation criteria in the framework of x-FEM-based structural analyses, Int. J. Numer. Anal. Methods Geomech. 31 (2007) 239–259.
[63] J. Unger, S. Eckardt, C. Könke, Modelling of cohesive crack growth in concrete structures with the extended finite element method, Comput. Methods Appl. Mech. Engrg. 196 (2007) 4087–4100.
[64] M. Cervera, G. Barbat, M. Chiumenti, Finite element modeling of quasi-brittle cracks in 2D and 3D with enhanced strain accuracy, Comput. Mech. 60 (5) (2017) 767–796.
[65] M. Nooru-Mohamed, Mixed-Mode Fracture of Concrete: an Experimental Approach (Ph.D. thesis), Delft University of Technology, 1992.
[66] Y. Zhang, R. Lackner, M. Zeiml, H. Mang, Strong discontinuity embedded approach with standard SOS formulation: element formulation, energy-based crack-tracking strategy, and validations, Comput. Methods Appl. Mech. Engrg. 287 (2015) 335–366.
[67] R. Peerlings, R. de Borst, W. Brekelmans, J. de Vree, Gradient-enhanced damage for quasi-brittle materials, Internat. J. Numer. Methods Engrg. 39 (1996) 3391–3403.
[68] L. Poh, G. Sun, Localizing gradient damage model with decreasing interactions, Internat. J. Numer. Methods Engrg. 110 (2017) 503–522.
[69] G. Sun, L.H. Poh, Homogenization of intergranular fracture towards a transient gradient damage model, J. Mech. Phys. Solids 95 (2016) 374–392.
[70] E. Martínez-Pañeda, A. Golahmar, C.F. Niordson, A phase field formulation for hydrogen assisted cracking, Comput. Methods Appl. Mech. Engrg. 342 (2018) 742–761.